Controlling photothermal forces and backaction in nano-optomechanical resonators through strain engineering

Menno H. Jansen,† Cauê M. Kersul,‡ and Ewold Verhagen*,†

†*Center for Nanophotonics, AMOLF, Science Park 104, 1098 XG, Amsterdam, The Netherlands*

‡*Centro de Tecnologia da Informação Renato Archer, Campinas 13069-901, Brazil*

E-mail: verhagen@amolf.nl

Abstract

In micro- and nanoscale optomechanical systems, radiation pressure interactions are often complemented or impeded by photothermal forces arising from thermal strain induced by optical heating. We show that the sign and magnitude of the photothermal force can be engineered through deterministic nanoscale structural design, by considering the overlap of temperature and modal strain profiles. We demonstrate this capability experimentally in a specific system: a nanobeam zipper cavity by changing the geometry of its supporting tethers. A single design parameter, corresponding to a nanoscale geometry change, controls the magnitude of the photothermal backaction and even its sign. These insights will allow engineering the combined photothermal and radiation pressure forces in nano-optomechanical systems, such that backaction-induced linewidth variations are deterministically minimized if needed, or maximized for applications that require cooling or amplification at specific laser detuning.

Keywords

optomechanics, nanomechanics, photothermal forces, strain engineering, radiation pressure, optical heating

1 Introduction

Cavity optomechanics offers powerful mechanisms for controlling mechanical resonators via light, with applications ranging from precision sensing[1–5] to quantum information processing.[6–9] Specifically, the dissipation and occupation of mechanical resonators can be controlled through dynamical backaction, leading to cooling or amplification.[10–13] By harnessing this effect, ground state cooling of macroscopic mechanical resonators has been demonstrated.[14,15] Traditionally, radiation pressure and, for higher frequency mechanics, electrostriction have been considered the primary forces mediating the interaction between optical and mechanical degrees of freedom.[16] However, the confinement of the optical field used to achieve large optomechanical coupling means that in many systems there are significant photothermal forces, arising from the strain produced by thermal expansion due to local heating.[17–26] These photothermal forces have even been used to implement advanced nanophotonic functionalities including phonon lasers and polarization control.[27,28] A better understanding of photothermal forces could allow their maximization or minimization, expanding the level of control in optomechanical application scenarios in both the classical and quantum domains.

In photonic cavities, backaction that modifies the mechanical response arises from optical forces that depend on mechanical displacement. Photothermal forces differ fundamentally from radiation pressure forces in how they affect mechanical dissipation, as a result of the different temporal dynamics of the mechanisms involved. The in-phase component of these forces affects the mechanical frequency, while the out-of-phase component can affect the dissipation. The ratio between these components depends on their delay in responding to a change in mechanical position.[16] Whereas radiation pressure relies on the photon lifetime to introduce a delay, the photothermal out-of-phase component arises from slower thermal time constants. This makes it particularly potent in low-frequency mechanical systems in the unresolved sideband regime, where it can dominate the linewidth variation from radiation pressure.[29] The photothermal force has even been argued to be able to achieve ground-state cooling in absorption-limited cavities.[21] Additionally, optical heating can introduce frequency shifts with a detuning dependence that differs from that expected from pure optomechanical backaction.

Cancellation of the photothermal force has been investigated using an optically levitated mirror,[30] but the sensitive interplay of optical, thermal, and mechanical strain fields in integrated systems opens avenues for more precise engineering. Recently, it has been argued that photothermal backaction can be predicted by evaluating the spatial overlap between thermal fields and the strain profiles of mechanical eigenmodes, and shown that this corresponds well to experimentally found values.[31]

The question is whether such understanding of the origin of this force can be leveraged to deterministically manipulate it, controlling its sign and magnitude at will. In this work, we show that by engineering the geometry of a nanoscale optomechanical device, the sign and magnitude of the photothermal force can be deterministically controlled. This can be achieved through subtle design changes that do not affect the essential optical and mechanical performance of the device. To this end, we first briefly discuss the theory of photothermal effects in optomechanical devices in terms of modal fields. We then use this to simulate the photothermal forces in a model system, a nanobeam zipper cavity, revealing symmetries that can be broken and exploited to manipulate the photothermal force. Finally, we show experimentally that breaking strain symmetry indeed allows the tuning of the photothermal force. We observe that optomechanical dissipation depends strongly on design, and can in fact be completely reversed. This opens a new degree of freedom for the design of nano-optomechanical systems, that could be employed in many different material and cavity design platforms.

2 Results and discussion

2.1 Photothermal and radiation pressure backaction

In an optomechanical device, there are multiple pathways for position fluctuations of the mechanical resonator to generate a force that acts back on the resonator. Two of these, through the radiation pressure and photothermal force, are schematically introduced in Figure 1a. We clarify that with the term 'radiation pressure', in this work we denote the combined forces associated with the moving boundary effect (in some other works exclusively referred to as radiation pressure) and the photoelastic effect (electrostriction). These can be calculated in a single perturbation-theory formalism, from a proper overlap integral of the optical and mechanical mode profiles.[32]

Both photothermal and radiation pressure backaction cycles can be understood starting with optomechanical transduction; fluctuations in the mechanical displacement, denoted in the frequency domain by $\delta x(\omega)$ in Figure 1a, lead to fluctuations in the frequency of the optical mode $\delta\omega_{\mathrm{o}}(\omega) = G_x \delta x(\omega)$, where G_x is the optomechanical coupling. Considering that the optical mode is driven by a laser at constant frequency, the resulting detuning fluctuations, $\delta\Delta(\omega)$, will affect the number of photons, $\delta n_{\mathrm{ph}}(\omega) = \Psi(\omega,\Delta) G_{\mathrm{x}} \delta x(\omega) n_{\mathrm{ph}}$, where $\Psi(\omega,\Delta) = ((\Delta+\omega)+i\kappa/2)^{-1} + ((\Delta-\omega)-i\kappa/2)^{-1}$ is the symmetrized optical susceptibility, whose imaginary part is related to the optical delay τ_o given by the inverse of the optical mode decay rate, κ^{-1}. In the case of radiation pressure backaction, these photon number fluctuations generate a fluctuating force that is also proportional to G_x, being the converse effect to the transduction. Upon joining all steps, the overall radiation pressure backaction force can be written as:

$$F_{\mathrm{rp}}(\omega) = \hbar G_{\mathrm{x}}^2 \Psi(\omega,\Delta) \delta x(\omega) n_{\mathrm{ph}}. \tag{1}$$

In addition to the radiation pressure force, $\delta n_{\mathrm{ph}}(\omega)$ leads to fluctuations in the absorbed number of photons, proportional to the optical absorption rate κ_{abs}, which in turn causes

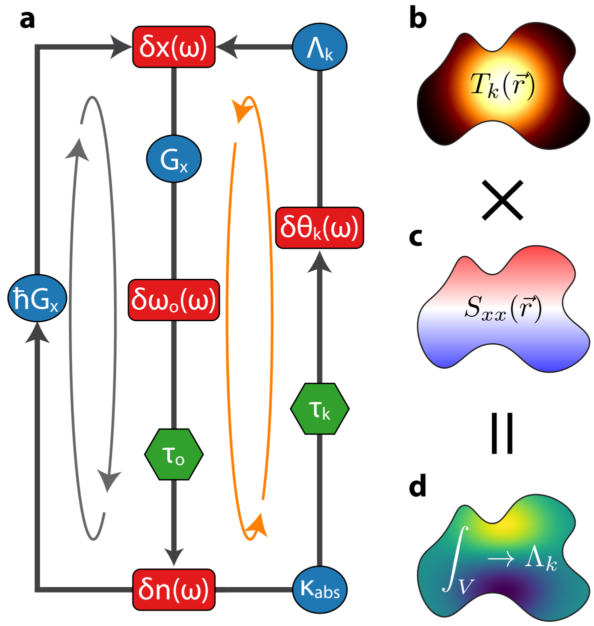

Figure 1: **a** Schematic of the radiation pressure (grey) and photothermal (orange) backaction cycles, with coupling rates displayed in blue ellipses, delay time constants in green hexagons and resulting dynamical variables in red rectangles. **b**, **c**, and **d** Schematic examples of a temperature profile $T_k(\vec{r})$, strain component $S_{xx}(\vec{r})$, and the integrand of Equation 6 resulting from their multiplication.

temperature fluctuations across the device. These temperature fluctuations will cause thermal strain, which can drive the mechanical mode of interest;[31]

$$m_{\text{eff}}\left(\delta\ddot{x} + \Gamma\delta\dot{x} + \Omega^2\delta x\right) = \int \boldsymbol{S}^x(\vec{r}) \colon \left(\boldsymbol{c} \colon \boldsymbol{S}^\theta(\vec{r}, t)\right) dV, \tag{2}$$

where m_{eff}, Γ, and Ω are its effective mass, decay rate, and angular frequency, $\boldsymbol{c}$ is the stiffness tensor of the medium, the operator ":" is the tensor contraction operation, $\boldsymbol{S}^x(\vec{r})$ is the normalized strain profile of the mechanical mode of interest and $\boldsymbol{S}^\theta(\vec{r}, t)$ is the thermal strain profile, which is given by

$$\boldsymbol{S}^\theta(\vec{r}, t) = \boldsymbol{\alpha}\delta T(\vec{r}, t), \tag{3}$$

where $\boldsymbol{\alpha}$ is the thermal expansion tensor and $\delta T(\vec{r}, t)$ is the temperature fluctuation profile. In the treatment of the photothermal effects, one should perform a multimodal expansion of the thermal field, which is discussed more thoroughly in section S5 of the Supporting Information. The end result of this expansion is a description of the temperature field $\delta T(\vec{r},t)$ in terms of thermal eigenmodes $\tilde{T}_k(\vec{r})$ and time dependent amplitudes $\delta\theta_k(t)$:

$$\delta T(\vec{r},t) = \sum_k \delta\theta_k(t)\tilde{T}_k(\vec{r}). \tag{4}$$

Considering here only the k-th thermal mode, one can solve the coupled dynamic equations in frequency space, see also section 5 of the Supporting Information, and obtain an expression for the amplitude of the fluctuations, given by

$$\delta\theta_k(\omega) = R_k^\theta \chi_k^\theta(\omega)/\tau_k \cdot \delta n_{\mathrm{ph}}(\omega), \tag{5}$$

where R_k^θ is a thermal resistance that depends on the overlap between the optical and thermal fields, derived in more detail in section 5 of the Supporting Information, τ_k is the thermal response time and $\chi_k^\theta(\omega) = (\tau_k^{-1} - i\omega)^{-1}$ is the thermal susceptibility, responsible for introducing the extra thermal delay, given by τ_k. Finally, $\delta\theta_k(\omega)$, leads to a contribution to the photothermal force $F_{\mathrm{pt},k}(\omega) = \Lambda_k \delta\theta_k(\omega)$, where Λ_k is the thermo-elastic coupling, defined as:

$$\Lambda_k^\theta = \int \mathbf{S}^x(\vec{r}) : (\mathbf{c} : \boldsymbol{\alpha})\, \tilde{T}_k(\vec{r})\, dV. \tag{6}$$

In Figure 1b, c, and d we present, respectively, schematic examples of $\tilde{T}_k(\vec{r})$, a component $S_{xx}(\vec{r})$ of $\mathbf{S}^x(\vec{r})$, and the resulting integrand of Equation 6.

Summing over all thermal modes, the photothermal force can be written as:

$$F_{\mathrm{pt}}(\omega) = \hbar G_x G_{\mathrm{pt}}(\omega) \Psi(\omega,\Delta) \delta x(\omega) n_{\mathrm{ph}}, \tag{7}$$

where $G_{\mathrm{pt}}(\omega) = \omega_0 \kappa_{\mathrm{abs}} \sum_k \left(\Lambda_k^\theta R_k^\theta \chi_k^\theta(\omega)/\tau_k\right)$ is the photothermal equivalent to G_x, with one fundamental difference: $G_{\mathrm{pt}}(\omega)$ carries an extra phase delay. Applying Equation 6 to the definition of $G_{\mathrm{pt}}(\omega)$ and performing the sum over all thermal modes, we can define it in terms of the profile of thermal fluctuations, $\delta T(\vec{r},\omega) = \sum_k \left(\tilde{T}_k(\vec{r}) R_k^\theta \chi_k^\theta(\omega)/\tau_k\right)$:

$$G_{\rm pt}(\omega) = \omega_0 \kappa_{\rm abs} \int \mathbf{S}^x(\vec{r}) : (\mathbf{c} : \boldsymbol{\alpha})\, \delta T(\vec{r},\omega)\, dV. \tag{8}$$

The sign of $F_{\rm om}(\omega)$ is uniquely given by $\Psi(\omega,\Delta)$, as it further depends only on G_x^2, which is always positive. This is not the case for $F_{\rm pt}(\omega)$, with its overall sign also affected by the relative sign between $G_{\rm pt}(\omega)$ and G_x. The ability to control the thermoelastic coupling Λ_k^θ, and consequentially $G_{\rm pt}(\omega)$, through the geometry of the device is precisely what we explore here to achieve deterministic control over the photothermal force: By controlling the overlap of the fields $\mathbf{S}^x(\vec{r})$ and $\delta T(\vec{r},\omega)$, the integral of Equation 6 can be drastically changed. Specifically, as we will see, both fields can have approximately orthogonal symmetries in realistic devices. A small breaking of symmetry through structural design can then lead to large changes of the backaction.

2.2 Photothermal forces in zipper cavities

As shown by Equation 8, we can engineer either the thermal strain field, $\boldsymbol{\alpha}\,\delta T(\vec{r},\omega)$ or the mechanical eigenmode strain field, $\mathbf{S}^x(\vec{r})$, to manipulate the photothermal force. Here we present an example of such engineering capability by breaking the symmetry of the mechanical strain field in a photonic crystal zipper cavity. The simulations required for this engineering were performed using the finite element method (FEM) program COMSOL Multiphysics.[33]

Zipper cavities are composed of two suspended nanobeams with elliptical holes, as shown in Figure 2b. In a single beam, the optical modes are confined within the central region by a quasi-1D photonic crystal, in which a defect is introduced by changing the spacing and the size of the ellipses.[34] As the nanobeams are brought together, their modes hybridize, giving origin to even and odd supermodes.[35–37] In our device, these are situated around 196THz. As the gap decreases, the frequency of the even mode decreases, while the frequency of the odd mode increases.

Due to the supporting tethers, the flexural mechanical modes of the nanobeams also hybridize.[38] The fundamental odd mode shown in Figure 2b presents a very high g_0, due to its modulation of the gap between the nanobeams. For a gap of 200nm $g_0/2\pi$ is around -150kHz for the even mode and $+30$kHz for the odd mode.

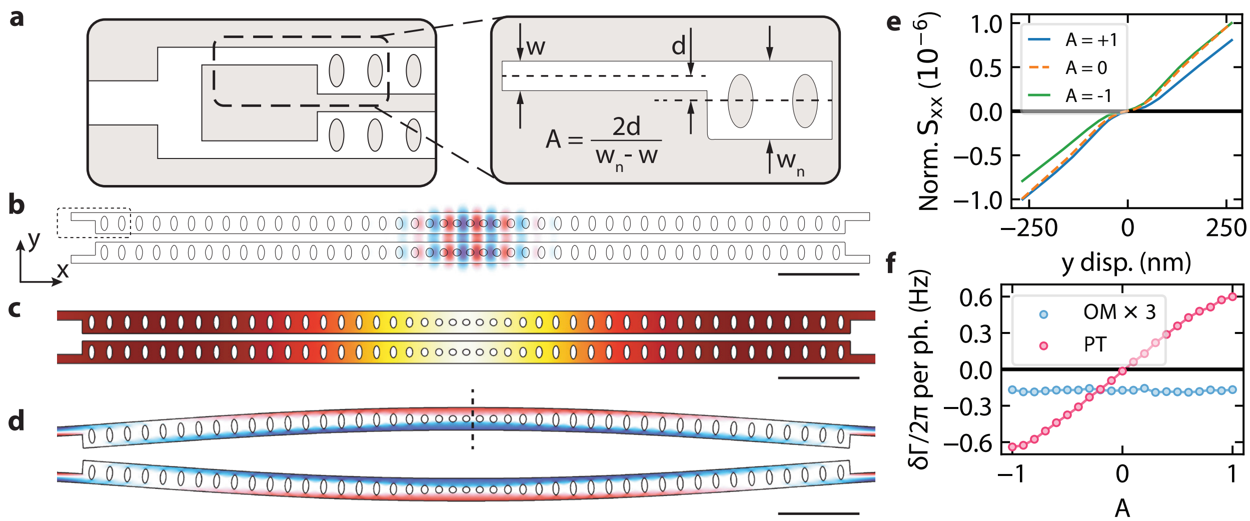

Figure 2: **a** Definition of the tether asymmetry, A, in terms of other tether parameters. The shown example is the case of $A = +1$. More examples are shown in Figure 3. **b** Electric field in the y direction for the even optical mode with frequency 196THz with a 2 µm scale indicated by the black line. **c** Imaginary part of the thermal fluctuations at the mechanical frequency. **d** S_{xx} stress component for the odd mechanical mode with frequency 5 6MHz. **e** Component S_{xx} of the normalized strain profile for different values of A evaluated at the cut-line shown by the dashed line in **d**. **f** In red and blue we have, respectively, the expected maximal linewidth variation, given by Equation 9, at the blue side of the resonance due to photothermal and radiation pressure effects, assuming typical experimental parameters for our devices and considering a temperature of 30K, where the silicon expansion coefficient is negative. As the the radiation pressure contributions are small we scaled it by a factor of 3 to improve the graph readability.

The radiation pressure coupling arises from the overlap of the optical field and mechanical displacement, while the thermo-elastic one arises from the overlap of the thermal and mechanical strain fields, as shown in Equation 8. By changing the positioning of the supporting tethers, we can significantly affect the mechanical strain while keeping the optical and thermal fields constant. In our device, this can be achieved through the displacement of the tether with respect to the center line of the nanobeam, d, shown in Figure 2a, with which we define the dimensionless tether asymmetry, $A = 2d/(w - w_n)$.

In Figure 2c the imaginary part of the temperature fluctuation profile, $\delta T(\vec{r}, \Omega)$, is shown, as it is the part related to variations on the mechanical linewidth. Across the short transversal direction, heat is evenly spread, while across the longer longitudinal direction, it is mostly concentrated near the optical mode, as heat does not have enough time to homogenize during a mechanical period; $\Omega\tau_k \gg 1$ for all the relevant thermal modes. The mechanical strain profile, shown in Figure 2d, is dominated by the S_{xx} component, which presents compressive stress in the inner part of the nanobeams and tensile stress in the outer part (for outwards displacement), with a neutral line close to the center of the nanobeam. For $A = 0$ the strain field has an almost perfect odd distribution in the y-direction with respect to the center line of a single nanobeam, as shown by the orange dashed line in Figure 2e, while the temperature profile presents an even distribution leading to an odd integrand in Equation 8 such that the photothermal coupling is approximately zero; $G_{\mathrm{pt}}(\Omega) = 0$.

Crucially, by changing the asymmetry A of the tether, we can control the intensity of the strain at the inner and outer edges of the nanobeam, as shown by the blue and green lines in Figure 2e. The temperature profile remains almost completely unchanged, since it does not reach the tether region. This combination breaks the symmetry in Equation 8, allowing for the control of photothermal effects.

As the tether approaches one extremity, the strain increases at the opposite edge. For $A = 1$, the strain at the inner edge ($y < 0$ in the graph) is larger in absolute terms than at the outer edge. This symmetry breaking mechanism is the dominant factor in the thermoelastic coupling, showing that by changing A we can have a positive or negative photothermal force. In other words, if there is thermal expansion with $A = 1$, the inner edge will expand more, as the outer edge is constrained by the tethers. This will bend the device inward, bringing the two nanobeams closer together.

By controlling the sign of the thermo-elastic coupling we control the sign of the linewidth variation, given by

$$\delta\Gamma = \frac{-1}{m_{\text{eff}}\Omega}\mathrm{Im}\left[\Sigma^{\text{RP}}(\Omega,\Delta)+\Sigma^{\theta}(\Omega,\Delta)\right], \tag{9}$$

as derived in detail in section 5 of the Supporting Information, with

$$\Sigma^{\text{RP}}(\omega,\Delta) = \hbar(G_x)^2\Psi(\omega,\Delta)n_{ph}, \tag{10a}$$

$$\Sigma^{\theta}(\omega,\Delta) = \hbar\omega_0\kappa_{\text{abs}}\sum_k \frac{R_k^\theta\Lambda_k^\theta\chi_k^\theta(\omega)}{\tau_k}G_x\Psi(\omega,\Delta)n_{ph}. \tag{10b}$$

The result is shown in Figure 2f, where the calculated absolute maximal linewidth variation at the blue detuned side, occurring at $\Delta = \kappa/(2\sqrt{3})$, is shown as a function of A. As expected in the sideband non-resolved regime, the linewidth variation induced by radiation pressure forces is small and does not depend on A, while the effects of photothermal forces, more or less proportional to A, are dominant, showing that changing the tether asymmetry allows tuning from amplification to cooling.

The length and width of the tethers are also relevant for the photothermal force. If the tethers are either too rigid or too compliant, the asymmetry effect is gradually lost, leading to small photothermal effects. As we increase the tether length, the mechanical frequency drops, and both radiation pressure and photothermal effects fall. Nevertheless, the latter are less affected in such a way that the ratio between photothermal and radiation pressure effects increases. In real devices, residual stress is another important aspect to consider as it can lead to large lateral warping of devices with asymmetric tethers, changing the intended gap between the nanobeams, and even leading to the collapse of the devices.

2.3 Experimental verification

Using our model as a guide, we fabricate and characterize zipper cavities with varying asymmetrical tether positions, examples of which are shown in Figure 3a, b, and c. The details of the fabrication procedure are given in section 1 of the Supporting Information. We characterize the devices in a closed-loop cryostat at 30 K using optical heterodyne detection. Light is side-coupled to the nanocavities using an on-chip waveguide, that is interfaced to a lensed optical fiber at the side of the chip. The setup is described in section 3 of the Supporting Information.

Simulations of the symmetric and anti-symmetric hybridized cavity mode profiles, which are the same for all tether asymmetries due to their insensitivity to A, are shown in Figure 3d and k, respectively. For each device, we step the laser wavelength over either of the optical resonances, and record a mechanical spectrum at each wavelength. From these spectra, the frequency and linewidth of the mechanical resonator can be determined through fitting the Lorentzian thermomechanical spectra. The results are shown in Figure 3e - j for the symmetric and Figure 3l - q for the anti-symmetric optical mode.

The main source of noise in the data stems from the limited integration time of the measurement, yielding a slight variation of the noise floor in each frequency bin, leading to uncertainty on the fitted frequencies and, more significantly, linewidths. Additionally, a drift can be seen in some of the measurements, likely originating from small temperature drifts of the setup. These effects are however small relative to the effects we are looking to study and exploit.

Before we continue with further quantitative analysis, we can immediately see some striking effects in Figure 3. Firstly, the sign of the linewidth variation $\delta\Gamma$ is opposite for the optical modes with opposite symmetries, giving a first indication that our backaction is likely photothermal in nature, as discussed at the end of subsection 2.1 and seen in Equations 1 and 7. Secondly, the sign of the linewidth variation $\delta\Gamma$ is opposite for opposite tether asymmetry A, showing that we can indeed control the photothermal force. Finally, the magnitude of the

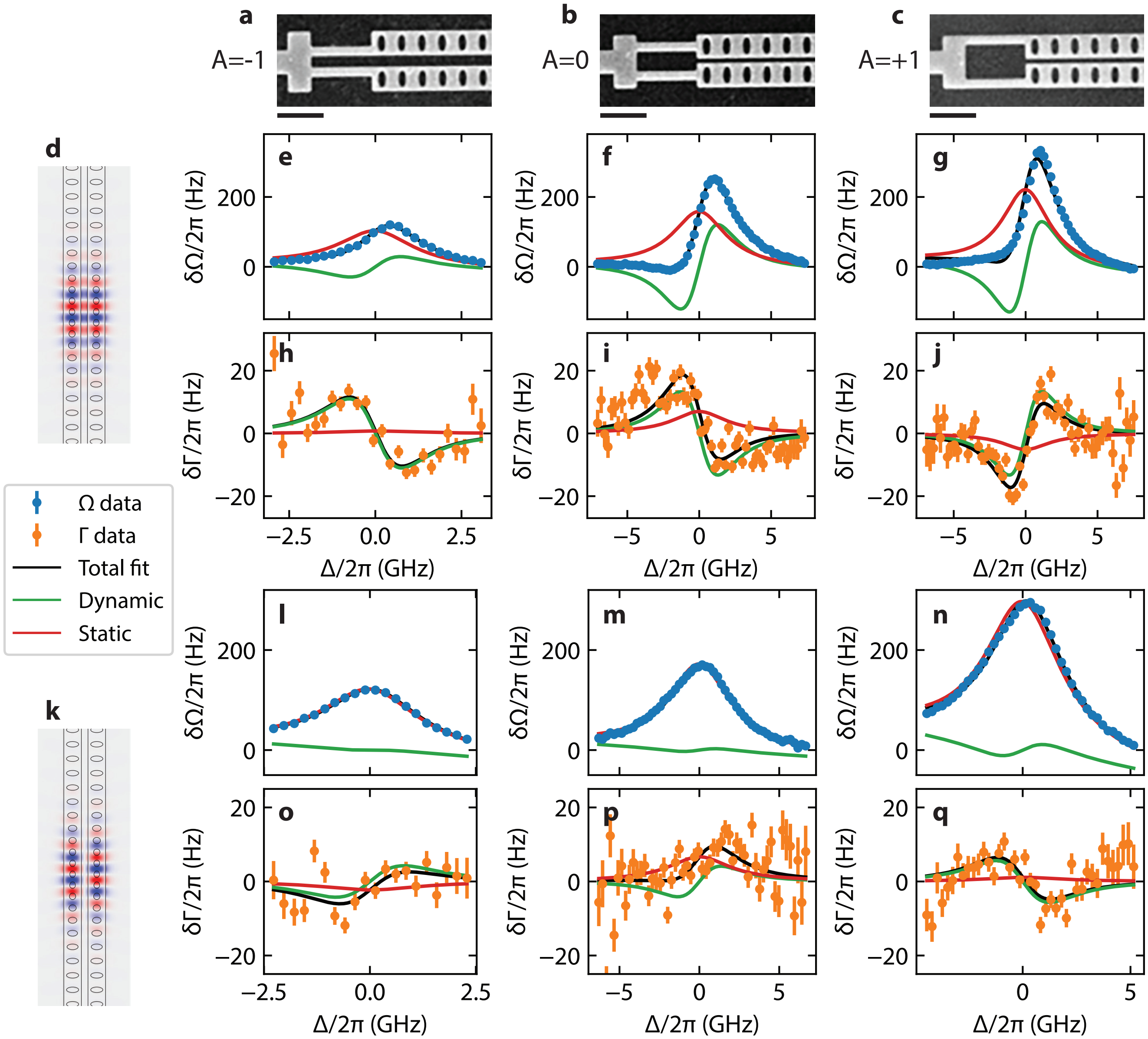

Figure 3: **a-c** SEM micrographs of the tethers of three fabricated devices, with 1 µm scale bar. **d**, **k** Simulated E_y mode profile of respectively the symmetric and anti-symmetric optical modes in the device. **e-g** (**h-j**) Measured frequency (linewidth) of the mechanical resonator as a function of optical detuning relative to the symmetric optical mode. Measured using respectively 17, 38, and 36 nW (A=-1, 0, +1) at the device. Measured data is indicated by the blue (orange) dots with error bars. The black line is the complete fit to Equation 11, with the red (green) line indicating the static (dynamic) contribution. **l-n** (**o-q**) Similar to **e-j**, but for the anti-symmetric optical mode.

frequency variations $\delta\Omega$ varies by a factor two to three, which can partially be explained by the difference in used input power, but indicates there are variations in device parameters that we must account for. This requires more quantitative analysis, which follows in the next few paragraphs.

The observed frequency and linewidth variations can be decomposed into static and dynamic contributions in the fit. The static components are purely due to the effects of the time-averaged local optical heating, $\kappa_{\mathrm{abs}} n_{\mathrm{ph}}(\Delta)$, causing a change of the local temperature, therefore they follow the same even squared Lorentzian function with respect to optical detuning Δ as $n_{\mathrm{ph}}(\Delta)$. The frequency of the mechanical mode increases due to the thermal contraction of the nanobeams[39] — the thermal expansion coefficient of silicon is negative at the temperatures used in our experiment.[40,41] The linewidth, in turn, is altered due to temperature-dependent mechanical loss mechanisms.[42]

The dynamic contributions are related to the movement of the mechanical resonator (hence their nomenclature), and originate from the backaction loops discussed in subsection 2.1.They are therefore proportional to the derivative of the cavity Lorentzian; $\partial n_{\mathrm{ph}}/\partial\Delta$, which is odd with respect to Δ. This leads to the following equations to fit to the experimental data:

$$\Omega(\Delta) = \Omega_0 + \delta\Omega_{\mathrm{drift}} \cdot \Delta + \delta\Omega_{\mathrm{dyn}} \cdot \frac{32}{3\sqrt{3}} \cdot \frac{\kappa^3 \cdot \Delta}{\left(4\Delta^2 + \kappa^2\right)^2} + \delta\Omega_{\mathrm{stat}} \cdot \frac{\kappa^2}{4\Delta^2 + \kappa^2} \tag{11a}$$

$$\Gamma(\Delta) = \Gamma_0 + \delta\Gamma_{\mathrm{dyn}} \cdot \frac{32}{3\sqrt{3}} \cdot \frac{\kappa^3 \cdot \Delta}{\left(4\Delta^2 + \kappa^2\right)^2} + \delta\Gamma_{\mathrm{stat}} \cdot \frac{\kappa^2}{4\Delta^2 + \kappa^2}, \tag{11b}$$

where the various terms have been normalized such that their maxima are equal to $\delta\{\Omega, \Gamma\}_{\{\mathrm{dyn,stat}\}}$, similar to the value given for $\delta\Gamma_{\mathrm{dyn}}$ in Figure 2f. Additionally, there is a term $\delta\Omega_{\mathrm{drift}}$ to account for small thermal drifts during the experimental sweep. The dynamic contributions can be related to the theory derived in subsection 2.1 through

$$\delta\Omega_{\mathrm{dyn}} = \frac{1}{2m_{\mathrm{eff}}\Omega} \mathrm{Re}\left[\Sigma_{\mathrm{om}}\left(\Omega, \frac{\kappa}{2\sqrt{3}}\right) + \Sigma_{\mathrm{pt}}\left(\Omega, \frac{\kappa}{2\sqrt{3}}\right)\right] \tag{12a}$$

$$\delta\Gamma_{\mathrm{dyn}} = \frac{-1}{m_{\mathrm{eff}}\Omega} \mathrm{Im}\left[\Sigma_{\mathrm{om}}\left(\Omega, \frac{\kappa}{2\sqrt{3}}\right) + \Sigma_{\mathrm{pt}}\left(\Omega, \frac{\kappa}{2\sqrt{3}}\right)\right], \tag{12b}$$

with

$$\Sigma_{\rm rp}(\omega,\Delta) = \hbar (G_x)^2 \Psi(\omega,\Delta) n_{\rm ph}(\Delta), \tag{13a}$$

$$\Sigma_{\rm pt}(\omega,\Delta) = \hbar G_{\rm pt}(\omega) G_x \Psi(\omega,\Delta) n_{\rm ph}(\Delta). \tag{13b}$$

The static contributions are limited to a phenomenological model as described above, but can still be used to infer information about effects that are proportional to temperature and time-averaged local heating.

As shown in Figure 2f, the photothermal force is expected to be the main source of dynamic linewidth variation $\delta\Gamma_{\rm dyn}$ in these unresolved sideband systems. Indeed, our experimental results show values 20 times higher than what would be expected from radiation pressure.

Using Equation 13, the ratio between the mechanical linewidth variation due to photothermal and radiation pressure forces is given by

$$\frac{\delta\Gamma_{\rm dyn,pt}}{\delta\Gamma_{\rm dyn,rp}} = \frac{\mathrm{Im}\left[G_{\rm pt}(\Omega)\right]}{G_x}\frac{\mathrm{Re}\left[\Psi\right]}{\mathrm{Im}\left[\Psi\right]} + \frac{\mathrm{Re}\left[G_{\rm pt}(\Omega)\right]}{G_x}. \tag{14}$$

In a sideband-unresolved mechanical resonator $\mathrm{Re}\left[\Psi\right]/\mathrm{Im}\left[\Psi\right] \approx \kappa/4\Omega \gg 1$. Recalling the definition of $G_{{\rm pt},k}(\Omega) = \omega_0 \kappa_{\rm abs} R_k^\theta \chi_k^\theta(\Omega) \Lambda_k^\theta/\tau_k$ we can examine the ratio between its real and imaginary parts. Using the fact that R_k^θ is proportional to τ_k and the assumption $1/\tau_k \ll \Omega$, which is true for all relevant thermal modes, we get $G_{{\rm pt},k}(\Omega) \propto (\Omega^2\tau_k)^{-1} + i/\Omega$. From this we see that $\mathrm{Im}\left[G_{{\rm pt},k}(\Omega)\right]/\mathrm{Re}\left[G_{{\rm pt},k}(\Omega)\right] \approx \Omega\tau_k \gg 1$. A more detailed discussion about the contributions of various thermal modes and their timescales can be found in section 5 of the Supporting Information and Figure S5.

For the sake of our discussion here we can lump all the relevant thermal modes using an effective thermal response time defined as $\tau_{\rm eff} = \mathrm{Im}\left[G_{\rm pt}(\Omega)\right]/\left(\mathrm{Re}\left[G_{\rm pt}(\Omega)\right]\cdot\Omega\right)$. As an example, for $A = 1$ we can calculate from simulation that $\Omega\tau_{\rm eff} = 10.1$, meaning $\tau_{\rm eff} = 297$ ns, in line with $\Omega\tau_{\rm eff} \gg 1$. Using $\kappa/2\pi \approx 4$ GHz and $\Omega/2\pi \approx 5$ MHz we arrive at $\mathrm{Im}\left[G_{\rm pt}(\Omega)\right]/G_x \sim 0.1$.

Using these values we can show that $(\mathrm{Im}\left[G_{\mathrm{pt}}(\Omega)\right]/G_x)\cdot(\mathrm{Re}\left[\Psi\right]/\mathrm{Im}\left[\Psi\right])\sim 20$, illustrating that the linewidth variation is dominated by the photothermal effect.

This result can also be used to estimate the ratio between the photothermal and radiation pressure contributions to the dynamic mechanical frequency variation, which is given by

$$\frac{\delta\Omega_{\mathrm{dyn,pt}}}{\delta\Omega_{\mathrm{dyn,rp}}} = \frac{\mathrm{Re}\left[G_{\mathrm{pt}}(\Omega)\right]}{G_x} - \frac{\mathrm{Im}\left[G_{\mathrm{pt}}(\Omega)\right]}{G_x}\frac{\mathrm{Im}\left[\Psi\right]}{\mathrm{Re}\left[\Psi\right]} \tag{15}$$

$$\approx \frac{\mathrm{Im}\left[G_{\mathrm{pt}}(\Omega)\right]}{G_x}\left(\frac{1}{\Omega\tau_{\mathrm{eff}}} - \frac{4\Omega}{\kappa}\right). \tag{16}$$

As $\mathrm{Im}\left[G_{\mathrm{pt}}(\Omega)\right]/G_x \sim 0.1$ and $((\Omega\tau_{\mathrm{eff}})^{-1} - 4\Omega/\kappa) \sim 0.1$ we can conclude that $\delta\Omega_{\mathrm{dyn,pt}}/\delta\Omega_{\mathrm{dyn,rp}} \sim 0.01$, confirming that the dynamical mechanical frequency variation is indeed dominated by radiation pressure effects.

As observed before in Figure 3, there are significant differences between measurements on different devices, in terms of input powers and device parameters. To allow a quantitative comparison of different physical devices, we repeat the procedure of sweeping the laser frequency over the optical resonances at various input powers. The slope $\beta_{\Gamma,\mathrm{dyn}} = \partial\delta\Gamma_{\mathrm{dyn}}/\partial n_{\mathrm{ph}|\Delta=0}$ of the dynamic linewidth variation $\delta\Gamma_{\mathrm{dyn}}$ to the number of photons at zero detuning $n_{\mathrm{ph}|\Delta=0}$ will allow us to compare $G_{\mathrm{pt}}(\Omega)$. The $\delta\Gamma_{\mathrm{dyn}}$ acquired from fitting to Equation 11b is shown as a function of the number of photons at zero detuning $n_{\mathrm{ph}|\Delta=0}$ for the symmetric optical mode in Figure 4b and for the anti-symmetric optical mode in Figure 4c, together with linear fits, performed using orthogonal distance regression (ODR). The other components and their fits are shown in Figure S3.

Importantly, the slope $\beta_{\Gamma,\mathrm{dyn}}$ depends on $|g_0|$ and κ_{abs}, which vary significantly between devices. In order to obtain a quantity related to the photothermal coupling, which can be easily compared between different devices, we normalize $\beta_{\Gamma,\mathrm{dyn}}$ by $|g_0|$ and κ_{abs}. Applying the definition $g_0 = G_x\sqrt{\frac{\hbar}{2\Omega m_{\mathrm{eff}}}}$ to Equation 11b and Equation 12b, within the relevant regime $\kappa \gg \Omega \gg \tau_{\mathrm{eff}}^{-1}$ we get:

$$\frac{\beta_{\Gamma,\mathrm{dyn}}}{|g_0|\kappa_{\mathrm{abs}}} = -\left(\sqrt{\frac{2\hbar}{\Omega m_{\mathrm{eff}}}}\,\mathrm{Im}\left[\Psi\left(\Omega, \frac{\kappa}{2\sqrt{3}}\right)\right]\right) \cdot \frac{g_0}{|g_0|}\frac{\mathrm{Im}\left[G_{\mathrm{pt}}(\Omega)\right]}{\kappa_{\mathrm{abs}}}, \tag{17}$$

where the first, bracketed, factor of this equation changes little between different devices, while the second term is the photothermal coupling normalized by κ_{abs}, multiplied by $\mathrm{sgn}\,(g_0)$.

To enable this, we can extract information about $|g_0|$ and κ_{abs} from the derivative of the dynamic and static frequency variation to the number of photons in the cavity, respectively.

In order to determine g_0, we assume, based on our previous discussion, that the dynamic frequency change $\delta\Omega_{\mathrm{dyn}}$, plotted as the green line in Figure 3e-g and l-n, is purely due to radiation pressure. The g_0 of each optical mode can then be extracted from the slope $\beta_{\Omega,dyn} = \partial\delta\Omega_{\mathrm{dyn}}/\partial n_{\mathrm{ph}|\Delta=0}$ of the dynamic frequency variation $\delta\Omega_{\mathrm{dyn}}$ to the number of photons at zero detuning $n_{\mathrm{ph}|\Delta=0}$, with $|g_0| = \sqrt{\frac{4}{3\sqrt{3}}\beta_{\Omega,dyn}\kappa}$, as detailed in section 4 of the Supporting Information and shown in Figure S3e and f. As we show in Table S3, we obtain reasonable agreement between experiment and simulation.

Determining κ_{abs} is generally difficult, as the temperature cannot be measured directly in our devices. While it is possible to extract this value from a nonlinear thermo-optic shift of the optical resonance, in conjunction with FEM simulations and the knowledge of the thermo-optical coefficient of the material,[31] we did not perform the equivalent characterization as in our case the nonlinear optical shift is dominated itself by static optomechanical effects. However, for small temperature changes δT, the static frequency variation $\delta\Omega_{\mathrm{stat}}$ is linearly proportional to δT,[39] which in turn is linearly proportional to the product $\kappa_{\mathrm{abs}} n_{\mathrm{ph}}$.[31] Therefore, we can use the slope $\beta_{\Omega,\mathrm{stat}} = \partial\delta\Omega_{\mathrm{stat}}/\partial n_{\mathrm{ph}|\Delta=0}$, shown in Figure S3g and h, as a proxy for κ_{abs}.

The static temperature profile is nearly independent from the tether asymmetry. As such, we assume here, that such static effects are independent from A. From the analysis of the static frequency variation for even and odd modes, shown in Figure S3, where data for different optical powers are presented, we do not observe any systematic trend attributable to A, confirming our assumption. Our data also shows that static effects are independent from

G_x, as can be verified from Figure 3, by comparing the static contributions to the frequency variation between the symmetric and anti-symmetric optical modes (Figure 3e and l, f and m, and g and n). These optical modes differ in G_x by approximately a factor of 5, but show very similar magnitude static components, taken at similar input powers. The variation of static effects between different devices is probably due to random variations of κ_{abs}

This static temperature change could potentially modify device parameters. A rough estimate of such heating can be obtained from the observed static mechanical frequency shifts, which go up to 200 Hz, assuming that these shifts are due to the stress induced by thermal contraction.[39] We used FEM simulations of the average thermal stress in the device to estimate that the frequency change due to thermal stress is around 5 kHz/MPa. Using a value of 169 GPa for the Young's modulus of silicon and 5.3×10^{-8} K^{-1} for its thermal expansion coefficient at 30K, we arrive at a maximal temperature variation on the order of 0.5K. This magnitude of heating should not change the heat capacity or thermal expansion coefficient significantly enough to affect our conclusions. Importantly, it does not significantly affect the comparisons between devices.

Finally, we are in a position to compare $G_{\mathrm{pt}}/\kappa_{\mathrm{abs}}$ between devices. To this end, we plot the normalized slope $\beta_{\Gamma,\mathrm{dyn}}/(|g_0|\beta_{\Omega,\mathrm{stat}})$ for all characterized geometries, as shown in Figure 4a.

Looking at the change in normalized $\beta_{\Gamma,\mathrm{dyn}}$ as a function of A, we see that the sign and magnitude of the variation in linewidth can be controlled by changing the tether asymmetry, as predicted in subsection 2.2. Comparing the results for even and odd optical modes, we see that the sign of the effect changes due to the change in the sign of g_0, while the magnitude of the effect remains the same, indicating that our normalized metric is indeed independent of g_0, as expected from photothermal effects.

Despite the clear qualitative agreement with the theory, we should note that according to our theory the $A = 0$ device is expected to have a very small linewidth variation, while this occurs in our experiments for slightly larger asymmetry $A \approx 0.5$. Because the non-

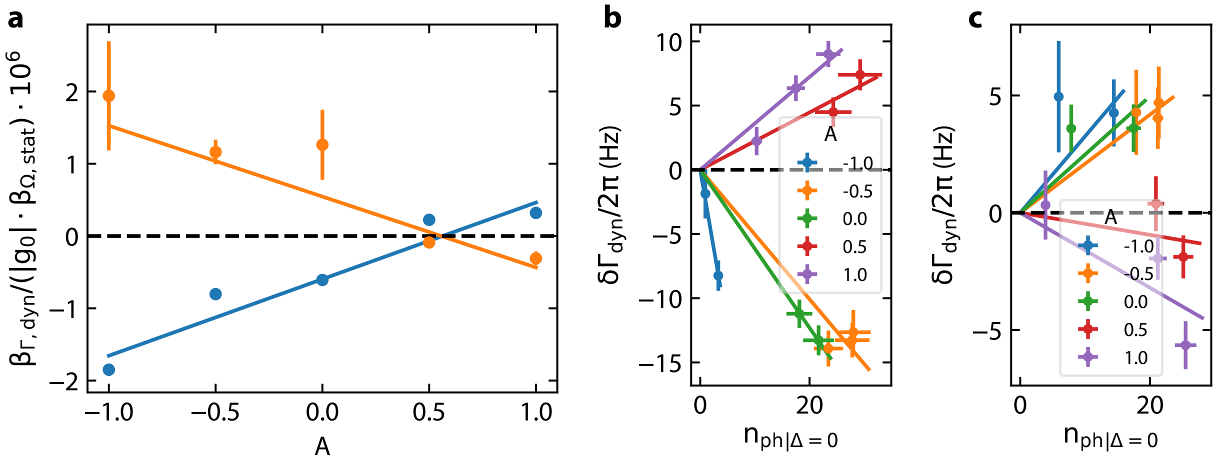

Figure 4: **a** The slope of the dynamic linewidth variation, $\beta_{\Gamma,\mathrm{dyn}} = \partial\delta\Gamma_{\mathrm{dyn}}/\partial n_{\mathrm{ph}}$, normalized by $|g_0|$ and $\beta_{\Omega,\mathrm{stat}}$, with a linear fit to the data for the symmetric (blue) and anti-symmetric (orange) optical modes. **b** (**c**) Measured dynamic linewidth variation for devices with various A for the symmetric (anti-symmetric) optical mode. Lines are linear fits to the data using ODR.

zero photothermal coupling originates from breaking the symmetry of the mechanical strain profile, this indicates that some other mechanism is inducing additional symmetry breaking.

Possible explanations could be an asymmetry in the sidewall properties between the inner and outer edges of the nanobeams due to different etch conditions in the gap. These could be the angle of the sidewall or the roughness of the surface. Assuming that we are close to the transition between ballistic and diffusive heat transport, even differences in roughness of the walls could lead to different effective temperatures. Finally, geometric asymmetry could also play a role, arising from a difference in alignment of the small asymmetric tethers with the long tethers to the substrate.

2.4 Conclusion

In summary, we showed that photothermal forces in nanoscale optomechanical devices can be controlled through strain engineering. We demonstrated this capability using the model system of a nanobeam zipper cavity. Using a theoretical model, we observed that the tether asymmetry strongly influences the strain profile across the nanobeams and thereby the thermoelastic overlap integral, while leaving the optomechanical coupling rate and mechanical frequency largely unaffected. Photothermal backaction is seen to depend very sensitively on geometrical parameters. For the same reason, we observed deviations due to inherent symmetry breaking, but geometrical control was seen to exceed that effect.

The ability to engineer photothermal forces enables a new degree of freedom in cavity optomechanics, allowing either suppression or enhancement of photothermal backaction. It could be used to suppress linewidth variation, thereby avoiding unwanted instabilities. Moreover, photothermal backaction could be maximized together with radiation pressure in optomechanical devices, leading to enhanced cooling and amplification performance in devices where purely optomechanical backaction is limited. This could allow the study of chaos in self-oscillating systems at lower input powers, or reaching stronger nonlinear regimes.[43] This enhancement of photothermal forces could also open up the exploration of macroscopic quantum mechanics with more massive mechanical resonators, which are usually deeply sideband-unresolved. It could allow studying the potential of photothermal forces for ground-state cooling in such systems, in regimes where regular radiation pressure backaction cooling is limited by the Doppler limit.[21]

Acknowledgement

The authors thank Thiago P. Mayer Alegre for the access to the computational infrastructure used for the simulations, as well as for the insightful discussions on the nature of the photothermal force.

This work is part of the research programme of the Netherlands Organisation for Scientific Research (NWO). It is supported by an NWO Vrij Programma (680-92-18-04) grant. It is furthermore funded by the European Union, supported by ERC Grant 101088055 (Q-MEME). Views and opinions expressed are however those of the authors only and do not necessarily reflect those of the European Union or the European Research Council Executive

Agency. Neither the European Union nor the granting authority can be held responsible for them.

C.M.K. acknowledges support by: São Paulo Research Foundation (FAPESP) through grants 18/15580- 6, 18/25339-4, 20/06348-2, 22/14273-8; Coordenação de Aperfeiçoamento de Pessoal de Nível Superior - Brasil (CAPES) (Finance Code 001); and Financiadora de Estudos e Projetos (Finep).

Supporting Information Available

Supporting Information: Fabrication details, device parameters, details of experimental setup, data analysis method, theoretical model, discussion of limits of model

Associated Content

Menno H. Jansen; Cauê M. Kersul; Ewold Verhagen. Controlling photothermal forces and backaction in nano-optomechanical resonators through strain engineering. 2025, arXiv:2512.21197. arXiv. https://doi.org/10.48550/arXiv.2512.21197 (accessed December 24, 2025).

References

(1) Krause, A. G.; Winger, M.; Blasius, T. D.; Lin, Q.; Painter, O. A high-resolution microchip optomechanical accelerometer. *Nature Photonics* **2012**, *6*, 768–772.

(2) Guha, B.; Allain, P. E.; Lemaître, A.; Leo, G.; Favero, I. Force Sensing with an Optomechanical Self-Oscillator. *Physical Review Applied* **2020**, *14*, 024079.

(3) Wu, M.; Wu, N. L.-Y.; Firdous, T.; Fani Sani, F.; Losby, J. E.; Freeman, M. R.; Barclay, P. E. Nanocavity optomechanical torque magnetometry and radiofrequency susceptometry. *Nature Nanotechnology* **2017**, *12*, 127–131.

(4) Yu, W.; Jiang, W. C.; Lin, Q.; Lu, T. Cavity optomechanical spring sensing of single molecules. *Nature Communications* **2016**, *7*, 12311.

(5) Gavartin, E.; Verlot, P.; Kippenberg, T. J. A hybrid on-chip optomechanical transducer for ultrasensitive force measurements. *Nature Nanotechnology* **2012**, *7*, 509–514.

(6) Barzanjeh, S.; Xuereb, A.; Gröblacher, S.; Paternostro, M.; Regal, C. A.; Weig, E. M. Optomechanics for quantum technologies. *Nature Physics* **2022**, *18*, 15–24.

(7) Riedinger, R.; Hong, S.; Norte, R. A.; Slater, J. A.; Shang, J.; Krause, A. G.; Anant, V.; Aspelmeyer, M.; Gröblacher, S. Non-classical correlations between single photons and phonons from a mechanical oscillator. *Nature* **2016**, *530*, 313–316.

(8) Zivari, A.; Fiaschi, N.; Burgwal, R.; Verhagen, E.; Stockill, R.; Gröblacher, S. On-chip distribution of quantum information using traveling phonons. *Science Advances* **2022**, *8*, eadd2811.

(9) Bozkurt, A. B.; Golami, O.; Yu, Y.; Tian, H.; Mirhosseini, M. A mechanical quantum memory for microwave photons. *Nature Physics* **2025**, 1–6.

(10) Kippenberg, T. J.; Rokhsari, H.; Carmon, T.; Scherer, A.; Vahala, K. J. Analysis of Radiation-Pressure Induced Mechanical Oscillation of an Optical Microcavity. *Physical Review Letters* **2005**, *95*, 033901, Publisher: American Physical Society.

(11) Wilson-Rae, I.; Nooshi, N.; Zwerger, W.; Kippenberg, T. J. Theory of Ground State Cooling of a Mechanical Oscillator Using Dynamical Backaction. *Physical Review Letters* **2007**, *99*, 093901, Publisher: American Physical Society.

(12) Marquardt, F.; Chen, J. P.; Clerk, A. A.; Girvin, S. M. Quantum Theory of Cavity-Assisted Sideband Cooling of Mechanical Motion. *Physical Review Letters* **2007**, *99*, 093902, Publisher: American Physical Society.

(13) Schliesser, A.; Rivière, R.; Anetsberger, G.; Arcizet, O.; Kippenberg, T. J. Resolved-sideband cooling of a micromechanical oscillator. *Nature Physics* **2008**, *4*, 415–419, Publisher: Nature Publishing Group.

(14) Teufel, J. D.; Donner, T.; Li, D.; Harlow, J. W.; Allman, M. S.; Cicak, K.; Sirois, A. J.; Whittaker, J. D.; Lehnert, K. W.; Simmonds, R. W. Sideband cooling of micromechanical motion to the quantum ground state. *Nature* **2011**, *475*, 359–363, Publisher: Nature Publishing Group.

(15) Chan, J.; Alegre, T. P. M.; Safavi-Naeini, A. H.; Hill, J. T.; Krause, A.; Gröblacher, S.; Aspelmeyer, M.; Painter, O. Laser cooling of a nanomechanical oscillator into its quantum ground state. *Nature* **2011**, *478*, 89–92, Publisher: Nature Publishing Group.

(16) Aspelmeyer, M.; Kippenberg, T. J.; Marquardt, F. Cavity optomechanics. *Rev. Mod. Phys.* **2014**, *86*, 1391–1452.

(17) Mertz, J.; Marti, O.; Mlynek, J. Regulation of a microcantilever response by force feedback. *Applied Physics Letters* **1993**, *62*, 2344–2346.

(18) Metzger, C. H.; Karrai, K. Cavity cooling of a microlever. *Nature* **2004**, *432*, 1002–1005.

(19) Favero, I.; Karrai, K. Optomechanics of deformable optical cavities. *Nature Photonics* **2009**, *3*, 201–205.

(20) Camacho, R. M.; Chan, J.; Eichenfield, M.; Painter, O. Characterization of radiation pressure and thermal effects in a nanoscale optomechanical cavity. *Optics Express* **2009**, *17*, 15726–15735.

(21) Restrepo, J.; Gabelli, J.; Ciuti, C.; Favero, I. Classical and quantum theory of photothermal cavity cooling of a mechanical oscillator. *Comptes Rendus. Physique* **2011**, *12*, 860–870.

(22) Woolf, D.; Hui, P.-C.; Iwase, E.; Khan, M.; Rodriguez, A. W.; Deotare, P.; Bulu, I.; Johnson, S. G.; Capasso, F.; Loncar, M. Optomechanical and photothermal interactions in suspended photonic crystal membranes. *Optics Express* **2013**, *21*, 7258–7275.

(23) Guha, B.; Mariani, S.; Lemaître, A.; Combrié, S.; Leo, G.; Favero, I. High frequency optomechanical disk resonators in III–V ternary semiconductors. *Optics Express* **2017**, *25*, 24639–24649.

(24) Hauer, B. D.; Clark, T. J.; Kim, P. H.; Doolin, C.; Davis, J. P. Dueling dynamical backaction in a cryogenic optomechanical cavity. *Physical Review A* **2019**, *99*, 053803.

(25) Shakespeare, C.; Kumar, A. S.; Muhonen, J. T. Thermal relaxation time and photothermal optomechanical force in sliced photonic crystal silicon nanobeams. *Optics Express* **2024**, *32*, 36824–36834.

(26) Ortiz, R.; Mercadé, L.; Grau, A.; Navarro-Urrios, D.; Martínez, A. Influence of thermal effects on the optomechanical coupling rate in acousto-optic cavities. *Physical Review A* **2024**, *109*, 023504.

(27) Navarro-Urrios, D.; Capuj, N. E.; Gomis-Bresco, J.; Alzina, F.; Pitanti, A.; Griol, A.;

Martínez, A.; Sotomayor Torres, C. M. A self-stabilized coherent phonon source driven by optical forces. *Scientific Reports* **2015**, *5*, 15733.

(28) Zanotto, S.; Tredicucci, A.; Navarro-Urrios, D.; Cecchini, M.; Biasiol, G.; Mencarelli, D.; Pierantoni, L.; Pitanti, A. Optomechanics of Chiral Dielectric Metasurfaces. *Advanced Optical Materials* **2020**, *8*, 1901507.

(29) Metzger, C.; Favero, I.; Ortlieb, A.; Karrai, K. Optical self cooling of a deformable Fabry-Perot cavity in the classical limit. *Physical Review B* **2008**, *78*, 035309.

(30) Qin, J.; Guccione, G.; Ma, J.; Gu, C.; Lecamwasam, R.; Buchler, B. C.; Lam, P. K. Cancellation of photothermally induced instability in an optical resonator. *Optica* **2022**, *9*, 924.

(31) Primo, A. G.; Kersul, C. M.; Benevides, R.; Carvalho, N. C.; Ménard, M.; Frateschi, N. C.; de Assis, P.-L.; Wiederhecker, G. S.; Mayer Alegre, T. P. Accurate modeling and characterization of photothermal forces in optomechanics. *APL Photonics* **2021**, *6*, 086101.

(32) Chan, J.; Safavi-Naeini, A. H.; Hill, J. T.; Meenehan, S.; Painter, O. Optimized optomechanical crystal cavity with acoustic radiation shield. *Applied Physics Letters* **2012**, *101*.

(33) COMSOL Multiphysics v6.2. 2023; `https://www.comsol.com`, COMSOL AB, Stockholm, Sweden.

(34) Deotare, P. B.; McCutcheon, M. W.; Frank, I. W.; Khan, M.; Lončar, M. High quality factor photonic crystal nanobeam cavities. *Applied Physics Letters* **2009**, *94*, 121106.

(35) Deotare, P. B.; McCutcheon, M. W.; Frank, I. W.; Khan, M.; Lončar, M. Coupled photonic crystal nanobeam cavities. *Applied Physics Letters* **2009**, *95*, 031102.

(36) Chan, J.; Eichenfield, M.; Camacho, R.; Painter, O. Optical and mechanical design of a "zipper" photonic crystal optomechanical cavity. *Optics Express* **2009**, *17*, 3802–3817.

(37) Eichenfield, M.; Camacho, R.; Chan, J.; Vahala, K. J.; Painter, O. A picogram- and nanometre-scale photonic-crystal optomechanical cavity. *Nature* **2009**, *459*, 550–555.

(38) La Gala, G.; Mathew, J. P.; Neveu, P.; Verhagen, E. Nanomechanical design strategy for single-mode optomechanical measurement. *Journal of Physics D: Applied Physics* **2022**, *55*, 225101.

(39) Schmid, S.; Villanueva, L. G.; Roukes, M. L. *Fundamentals of Nanomechanical Resonators*; Springer International Publishing: Cham, 2023.

(40) Vanhellemont, J.; Swarnakar, A. K.; Van Der Biest, O. Temperature Dependent Young's Modulus of Si and Ge. *ECS Transactions* **2014**, *64*, 283–292.

(41) Middelmann, T.; Walkov, A.; Bartl, G.; Schödel, R. Thermal expansion coefficient of single-crystal silicon from 7 K to 293 K. *Physical Review B* **2015**, *92*, 174113.

(42) Mohanty, P.; Harrington, D. A.; Ekinci, K. L.; Yang, Y. T.; Murphy, M. J.; Roukes, M. L. Intrinsic dissipation in high-frequency micromechanical resonators. *Physical Review B* **2002**, *66*, 085416.

(43) Navarro-Urrios, D.; Capuj, N. E.; Colombano, M. F.; García, P. D.; Sledzinska, M.; Alzina, F.; Griol, A.; Martínez, A.; Sotomayor-Torres, C. M. Nonlinear dynamics and chaos in an optomechanical beam. *Nature Communications* **2017**, *8*, 14965.

TOC Graphic